



HAL
open science

Comparison of techniques to localise U-bearing particles in environmental samples

Aurélie Diacre, Pascal Fichet, Paul Sardini, Jérôme Donnard, Anne-Laure Fauré, Olivier Marie, Katsumi Shozugawa, Michaël Susset, Mayumi Hori, Takizawa Tsutomu, et al.

► To cite this version:

Aurélie Diacre, Pascal Fichet, Paul Sardini, Jérôme Donnard, Anne-Laure Fauré, et al.. Comparison of techniques to localise U-bearing particles in environmental samples. *Journal of Radioanalytical and Nuclear Chemistry*, 2022, 331, pp.1701-1714. 10.1007/s10967-022-08229-w . cea-03600979

HAL Id: cea-03600979

<https://cea.hal.science/cea-03600979>

Submitted on 8 Mar 2022

HAL is a multi-disciplinary open access archive for the deposit and dissemination of scientific research documents, whether they are published or not. The documents may come from teaching and research institutions in France or abroad, or from public or private research centers.

L'archive ouverte pluridisciplinaire **HAL**, est destinée au dépôt et à la diffusion de documents scientifiques de niveau recherche, publiés ou non, émanant des établissements d'enseignement et de recherche français ou étrangers, des laboratoires publics ou privés.

Copyright

25 **Comparison of techniques to localise U-bearing particles in**
26 **environmental samples**

27 *Aurélie D.*^{1,2}, Pascal F.³, Paul S.⁴, Jérôme D.⁵, Anne-Laure F.¹, Olivier M.¹, Katsumi S.⁶,*
28 *Michaël S.¹, Mayumi H.⁶, Takizawa T.⁶, Fabien P.¹, Olivier E.²*

29 ¹*Commissariat à l'Energie Atomique et aux énergies alternatives (CEA, DAM, DIF, F-91297*
30 *Arpajon, France.*

31 ²*Laboratoire des Sciences du Climat et de l'Environnement (LSCE/IPSL), Unité Mixte de*
32 *Recherche 8212 (CEA/CNRS/UVSQ), Université Paris-Saclay, Gif-sur-Yvette, France.*

33 ³*DES-Service d'Etudes Analytiques et de Réactivité des Surfaces (SEARS), CEA, Université*
34 *Paris-Saclay, 91191, Gif-sur-Yvette, France.*

35 ⁴*Université de Poitiers, UMR CNRS 7285 IC2MP / HYDRASA, rue Michel Brunet, 86022,*
36 *Poitiers Cedex, France.*

37 ⁵*Ai4r, 2 Rue Alfred Kastler, 44307 Nantes, France.*

38 ⁶*The University of Tokyo, Graduate School of Arts and Sciences, Tokyo 153-8902, Japan.*

39

40

41 **Abstract**

42 This publication shows results of a comparison of three techniques for localising
43 radioactive, and U-bearing particles on same samples. Particles are localised by the means of three
44 methods: (1) Fission Tracks (FT), (2) Imaging Plate (IP), and (3) real time autoradiography
45 (BeaQuant[®]). These techniques were applied to various samples, including a sediment sampled in

46 the vicinity of the Fukushima Dai-Ichi Nuclear Power Plant (FDNPP) and a sample made of pure
47 U oxide particles. In addition, the efficiency of the combination of two methods (FT and IP) to
48 localise specifically anthropogenic U-bearing particles was tested.

49 **Key words**

50 BeaQuant[®], imaging plate, fission tracks, alpha and beta emitters localisation, uranium.

51 **1. Introduction**

52 Nowadays there is a real need for the detection and characterisation of anthropogenic
53 radioactive particles contained in soils/sediments to assess the exposure of human beings to
54 ionizing radiation and its consequences on health and the environment. These particles have been
55 emitted during nuclear accidents such as Chernobyl [1–3], Fukushima Dai-Ichi Nuclear Power
56 Plant (FDNPP) [4–16], Thulé [17, 18], and Palomares [19–21] or have been released from nuclear
57 facilities during nuclear fuel cycle operations [22]. Actinides are particularly interesting because
58 of their long persistence in the environment (24.11×10^3 years for ^{239}Pu to 4.47×10^9 years for
59 ^{238}U) and can therefore be used as a sediment tracer [23]. For accurate assessment of the
60 environmental impact of these particles and associated risks, it is important to be free from other
61 sources of actinides like natural uranium bearing minerals or global fallout from past nuclear
62 weapon tests. Thus when performing traditional bulk analysis on soil or sediment samples, the
63 resulting isotopic and elemental composition is a mixing of all these actinide sources. Only particle
64 analysis that consists in the characterisation at the particle scale enables to focus on the emission
65 source of interest.

66 The goal of this work is to investigate nuclear fuel-bearing particles and to study the
67 detection capacities of three techniques: (1) the fission track method, based on the fissile properties
68 of ^{235}U and ^{239}Pu , (2) real time α -autoradiography, based on the detection of α -emitting isotopes
69 (^{234}U , ^{235}U , ^{238}U , ^{239}Pu , ^{240}Pu) and (3) α -autoradiography on imaging plates. Since the 1990's, the
70 fission track method has been implemented for the detection of particles containing uranium and
71 plutonium in safeguards samples [24] and is very sensitive to high enriched uranium bearing
72 particles. In the field of medical biology and geosciences, a new real-time digital autoradiography
73 method is already in use, the BeaQuant[®] (Ai4R, Nantes, France). This device, implemented on
74 thin slides of rocks [25] and on biological samples, enables a quantitative chemical mapping of
75 alpha emitters. The last method based on the use of imaging plates is commonly used in the
76 literature to detect particles containing β - γ emitters [4–6, 8–16, 26, 27]. These β - γ emitters may
77 be actinide decay products or fission products such as ^{137}Cs if nuclear fuel has been irradiated. In
78 this paper, we implemented the imaging plate method developed by [27] to detect specifically α -
79 emitters.

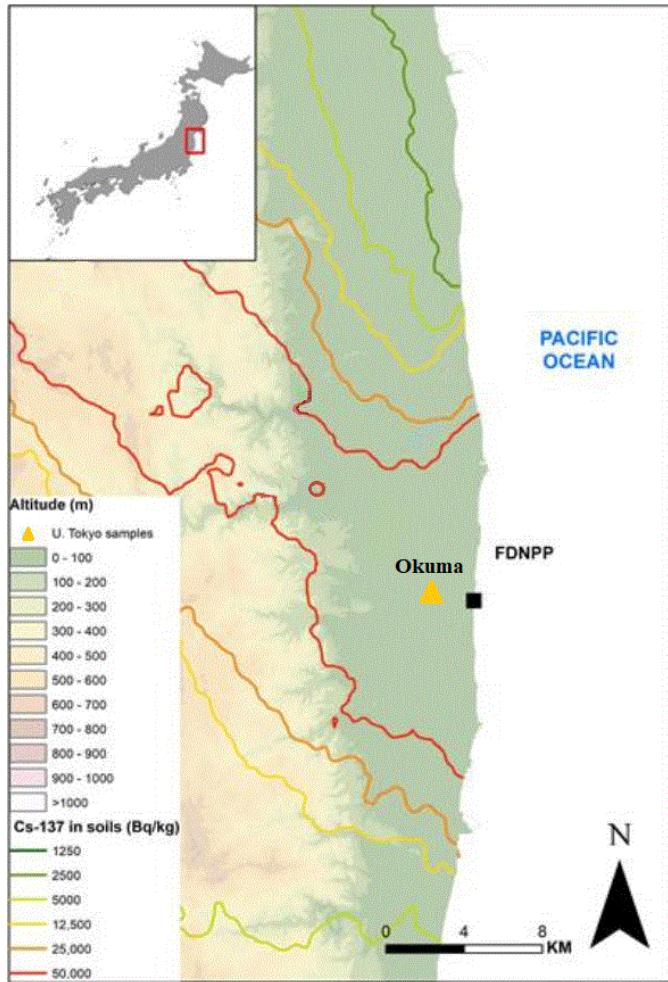
80 To our knowledge, these three detection-localisation techniques are compared for the first
81 time for two different types of samples: (1) pure U oxide micro-particles (highly enriched U with
82 a 40% atomic abundance of ^{235}U); and (2) a sediment sample collected in the vicinity of FDNPP
83 with significant ($> 10,000 \text{ kBq}\cdot\text{kg}^{-1}$) β and γ emitter activities that may contain nuclear fuel
84 particles. Besides, a grass sample (IAEA 472 CRM) that contains only β and γ emitters was also
85 prepared as a control sample. We also describe the different limitations of each method. Actually,
86 the presence of naturally occurring nuclides such as uranium (α emitter) and its decay products
87 (mainly β - γ emitters) in soils/sediments may hide the presence of anthropogenic particles
88 specifically in case of volcanic U-rich soils for example. Moreover, in the case of irradiated nuclear

89 particles, radioactive emissions from actinides are mostly negligible compared to the proportion
90 of β - γ emissions from fission products (^{137}Cs , etc.). The fission products may generate
91 interferences on α -autoradiography detection. In addition to this comparison exercise, theoretical
92 numbers of FT and α -tracks generated for the U-bearing particles from both samples (pure U and
93 FDNPP U-bearing particles) were calculated assuming given transmission and auto-adsorption
94 coefficients.

95 **2. Material and methods**

96 **2.1. Sample collection and preparation**

97 A sediment sample referred to as Okuma was collected at 2.7 km to the West of FDNPP,
98 in Choja-bara, Otto-zawa, Okuma Town, Fukushima Prefecture, Japan (37.42230°N 141.00345°E)
99 (**Fig. 1**) on March 18, 2014 within the Restricted Zone. The specific activity of ^{137}Cs was 13,300
100 $\text{kBq}\cdot\text{kg}^{-1}$ ($\pm 18 \text{ kBq}\cdot\text{kg}^{-1}$) at the time of analysis. About 1 g of the sample was dry-sieved to 63
101 μm . The sample fraction was then suspended in a mixture of ethanol and of an organic polymer
102 (collodion) and spread on Lexan[®] disks (Lexan[®], General Electric Plastic, USA). Coating with
103 collodion was necessary both to immobilize particles and to prevent contamination of the detection
104 media. Three disks referred to as 20B2, 20B16, and 20B20, were prepared and used for the
105 experiments. A process blank was also prepared with the same method.



106

107 **Fig. 1** Background ^{137}Cs level map in soils of the Fukushima prefecture after Chartin et al. (2013)
 108 with location of the Fukushima Dai-Ichi Nuclear Power Plant (FDNPP, black square) and the
 109 investigated sediment sample (yellow triangle).

110

111 Moreover, a subsample of the IAEA-472 certified material was also analysed as a control
 112 sample. This material, collected in Polesskoe, Kiev, Ukraine during summer in 1990, is a grass
 113 sample, which contains only β and γ emitters like ^{40}K and ^{137}Cs with a reference weight activity
 114 decay-corrected to 2020 of $1 \text{ kBq}\cdot\text{kg}^{-1}$ in ^{40}K and $8 \text{ kBq}\cdot\text{kg}^{-1}$ in ^{137}Cs . This standard sample was
 115 prepared using the same protocol as for the Okuma sample and dispersed onto two Lexan[®] disks

116 (1 mg, i.e. $\approx 4.1 \times 10^{-3}$ Bq of ^{137}Cs per disk). The analysis of this certified material was used to
117 estimate the contribution of β emissions during BeaQuant[®] acquisitions.

118 Finally, samples containing highly enriched uranium micro-particles (HEU MP) with a
119 ^{235}U atomic abundance of 40 % referred to as 19A32 and 19A33 were also used as a reference for
120 α -emitters because their specific α -activity (α -activity by mass unit) is higher than those of the
121 naturally-occurring (non-purified) U (by a factor of ~ 6) and of the U from reactor 3 (without Pu)
122 from FDNPP (by a factor of ~ 17). Therefore, we expect to have greater chances to detect such
123 pure HEU particles by α -autoradiography techniques instead of natural mineral particles rich in U
124 for the same U content. These particles, whose equivalent diameters range between 250 and 400
125 nm, were mixed with urban particulate matter (SRM 1648a, National Institute of Standards and
126 Technology, USA) that contains element like aluminium, silicon and lead which are expected to
127 be found in industrial environments. This SRM contains also natural U with an estimated
128 concentration about $5 \text{ mg}\cdot\text{kg}^{-1}$, which is slightly larger than the estimate of the average
129 concentration of U in soil ($\sim 3 \text{ mg}\cdot\text{kg}^{-1}$). The estimated mass of natural U was equal to about 16
130 ng and the mass of HEU equal to about 32 ng [29]. These particles were trapped in a piece of
131 cotton and were extracted from the cotton tissue in an ultrasonic bath filled with ethanol. After
132 mixing with the organic polymer, particles were deposited on Lexan[®] disks like the Okuma
133 sample.

134

135 **2.2. Methods for localising radioactive particles implemented in this study**

136 **2.2.1. Imaging Plates (IP) technique**

137 The imaging plate (IP) is a passive, two-dimensional radiation detector based on the photo-
138 stimulated luminescence (PSL) phenomenon [30, 31]. Due to their high sensitivity over a large

139 range of energy levels, IPs applications are widely used in medical and environmental sciences.
140 There are three types of IPs: (1) TR (Tritium), (2) MS (Multipurpose Standard), and (3) SR (Super
141 Resolution). Differences between these IP types are: (1) the absence of protective layers for the
142 TR type and (2) variable thickness of the sensitive layer between IP types. In all of them, the active
143 layer is made of a photo-stimulating phosphor crystal, typically BaF(Br,I):Eu²⁺ [31]. When
144 exposed to an ionizing radiation – energetic charged particles, X-rays, or γ rays – some of the
145 incoming ionizing particles deposit a part of their energy which is stored in the phosphorous layer
146 in the form of FBr⁻ or FI⁻ centres and Eu³⁺ ions [30]. The electrons that are trapped in these sites,
147 can be later released by visible light irradiation and reintegrated into the Eu³⁺ ions followed by the
148 emission of 3 eV photons called PhotoStimulated Light (PSL) [30]. The emitted light in the blue
149 part of the visible spectrum can be detected, usually by means of a photomultiplier tube (PMT),
150 and its intensity is proportional to the incident radiation intensity recorded in the IP [33] with a
151 very large dynamic range of intensity, typically spanning five orders of magnitude.

152 To be used as a detector, IP must be calibrated for both the PSL response to radiation (energy and
153 type) and for spatial resolution. The IP calibration is done with known activity sources and
154 different exposure times [34]. In this study, we implemented TR films (IP, TR 12.5 cm \times 25.2 cm,
155 Perkin Elmer) without a protective layer to increase the probability of detecting α emissions at
156 very low levels of activity from actinide-bearing particles. A methodology based on the overlay of
157 several IPs to try to identify different radioisotopes was developed [27]. Indeed, γ rays and
158 electrons can imprint several IPs depending on their energy while α particles can only impact the
159 first (closest to the same sample) IP. Here, we applied this method by overlaying two IPs to
160 discriminate the impact of β and γ versus α -particles. The IP in contact with prepared disks (IP1)
161 allows recording α , β and γ PSL and the second IP (IP2) allows recording of only γ and β PSL.

162 Therefore, PSL emissions observed only for IP1 and not for IP2, or significantly stronger for IP1
 163 than for IP2, are very likely to indicate that samples contain α -emitters.

164 Two disks of the Fukushima sample (Okuma) and two disks of the HEU MP were analysed
 165 with this device for an acquisition time of two weeks in the darkness in lead shielding
 166 (Supplementary information A). This acquisition time was set to improve the chance to detect
 167 alpha emission without much loss of sensitivity due to fading effect. Autoradiography images were
 168 then recorded using the IP reader (Cyclone Plus, Perkin Elmer) with a pixel size of 150 dpi (dot
 169 per inch) corresponding to one measurement each 169 μm in the IP screen. The IP reader quantified
 170 the radiation intensity as PSL for each pixel (a total of 749×1452 pixels) and stored it in a TIFF
 171 image format.

172 To identify high-radioactivity spots, the autoradiography images of IP1 (**Fig. 4a**) and IP2 (**Fig.**
 173 **4b**) were processed using the ImageJ software (<https://imagej.nih.gov/ij/>) in order to report the
 174 PSL values of each IP pixel in a table. Raw PSL values were corrected by the software's drift
 175 values of the IP reader (Eq. (1)).

$$176 \quad PSL_{Corrected\ IP1} = PSL^2 \times 2.34 \times 10^{-5} \quad (1)$$

177 For the IP2 the same calculation takes into account the loss factor of β - γ between the two IP, which
 178 determined to be 0.18 from a ^{137}Cs source [27] (Eq. (2)).

$$179 \quad PSL_{Corrected\ IP2} = PSL^2 \times 2.34 \times 10^{-5} / 0.18 \quad (2)$$

180 To highlight hot spots corresponding to α emissions only, the PSL-corrected values of the IP2 were
 181 subtracted from the PSL-corrected values of the IP1 (Eq. (3)).

$$182 \quad PSL_{1-2} = PSL_{Corrected\ IP1} - PSL_{Corrected\ IP2} \quad (3)$$

183 Finally, PSL_{1-2} was corrected for the background and the standard deviation (Eq. (4))

$$184 \quad PSL_{1-2} = PSL_{1-2} - mean_{background} - 3 \times RSD_{background} \quad (4)$$

185 Results of the processed IP PSL were then converted into a new autoradiography image with
186 ImageJ to visualize hot spot locations (**Fig. 4c**).

187

188 **2.2.2. Fission Tracks (FT) technique**

189 An additional Lexan[®] disk, acting as solid state nuclear track detector and referred to as
190 “FT disk”, was welded onto each Lexan[®] disk onto which the particulate sample was deposited
191 (referred to as “deposition” disk). The disks were then packed into a capsule and irradiated in the
192 TRIGA nuclear reactor (Jozef Stefan Institute, Ljubljana, Slovenia). A specific irradiation device
193 was used for that purpose in order to get a well-thermalized neutron flux with a high fluence, in
194 the 10^{15} neutron cm^{-2} range, to be able to detect particles with low numbers of fissile nuclei [35].
195 Fissile nuclides (^{235}U , ^{239}Pu) underwent a fission reaction during which two fission fragments were
196 emitted. These fragments then impacted the Lexan[®] disks and modified their surface structure [24].
197 After irradiation, the FT disk was chemically etched to make FT visible under an optical
198 microscope. The sea urchin-shaped FT clusters are characteristic of the presence of a fissile
199 nuclide-bearing particle. With appropriate landmarks on both deposition and revelation Lexan[®]
200 disks, it is possible to locate the particle that produced the FT cluster.

201 FT clusters may come from either (1) a mineral particle of significant size with a
202 sufficiently high content of naturally-occurring U (like zircons, monazite or granites), or (2) a
203 particle coming from the FDNPP which contains human-modified U (i.e. purified and enriched in
204 fissile ^{235}U isotope) and possibly ^{239}Pu (produced within the nuclear fuel by neutron capture or
205 initially added to UO_2 to make a MOX fuel). Once the particle localised, its source can be identified
206 by combining the determinations of the elemental composition from SEM-EDS and of the U
207 isotopic composition by secondary ion mass spectrometry.

208

209 **2.2.3. BeaQuant® technique**

210 The BeaQuant® is a digital autoradiography real-time acquisition system based on the use of a
211 gaseous detection medium [25, 36]. The micro-pattern gaseous detector (MPGD) incorporates a
212 micromesh parallel ionization multiplier (PIM) [37–39]. In this gas mixture, charged particle
213 emitted by the sample interact with the gas and release their energy by ionization of the gas
214 mixture. Exposed to appropriate electric fields, the electrons created during the interaction are
215 multiplied, drifted and sent to the segment anode. A α -disintegration triggering the electronic
216 acquisition is thus reported on an autoradiography image in real time. BeaQuant® has the capability
217 to count and map α or β -emitting particles without influence of γ emitters [25, 37] and with a high
218 spatial resolution (maximum resolution of 20 μm for both α and β from tritium detection [39, 40].
219 With the MPGD, the BeaQuant's® sensitivity is about $5 \times 10^{-5} \text{ cps} \cdot \text{cm}^{-2}$ for a U concentration of 2
220 ppm at secular equilibrium [25], with a detection linear response of 5 orders of magnitude [37].
221 Moreover, by adjusting the BeaQuant® amplification gains, it is possible to discriminate α and β
222 emissions.

223 However, samples analysed with BeaQuant® need to be perfectly flat: any surface
224 roughness can induce artefacts corresponding to artificial hot spots on the autoradiography image.
225 The sample preparation carried out in this study is therefore perfectly appropriate for BeaQuant®
226 analyses. Disks were placed during four days within a GS-1010 sample holder (10 cm \times 10 cm),
227 in front of the gas detector and analysed with the measurement parameters configured for ^{238}U in
228 order to detect α emitters (referred to as method 1) specifically. As Fukushima samples are highly
229 contaminated with ^{137}Cs ($>10 \text{ kBq} \cdot \text{kg}^{-1}$), a second acquisition was realized with a configuration
230 more restrictive on U energy in order to avoid ^{137}Cs detection (referred to as method 2). The

231 acquisition time was set to ten days because the sensitivity was reduced with these settings. The
232 IAEA-472 standard sample was also analysed by method 2 in order to check the decrease in
233 background due to the energy limitation. For method 2, the pixel size chosen for the analysis
234 reached up to 50 μm and increased to 400 μm after post-processing in order to integrate a stronger
235 signal per pixel.

236 After acquisition with both methods, post-processing was conducted to remove the β
237 contribution. Betas were identified by their significant contribution in the low amplitudes. The
238 filtering consisted of removing these low amplitude signals to keep the background noise as low
239 as possible.

240

241 **2.3. Morphological and elemental characterisation of the particles by SEM-EDS** 242 **(Scanning Electron Microscopy - Energy Dispersive Spectroscopy)**

243 A scanning electron microscope (FEI QuantaTM 3D FEG (Field Emission Gun), Eindhoven,
244 The Netherlands) equipped with backscattered and secondary electron detectors was used to
245 determine the size, the morphology and the elemental composition of the particles.
246 Elemental analyses on particles were realized in-situ via EDS with an Octane Elect Plus detector
247 (EDAX, Ametek, Tilburg, The Netherlands), which has a surface area of 30 mm². Analyses were
248 performed with an accelerating voltage of 30 kV to detect U X-ray at 13.6 keV.

249 **3. Results and discussion**

250 **3.1. Theoretical performance of the three methods**

251 Theoretical calculations were made to estimate the numbers of (1) α emissions and (2) FT
252 depending on the elemental/isotopic composition and the size of the particle. In this section, we

253 considered a pure UO₂ particle with a density of 10.97 g·cm⁻³ and a ²³⁵U abundance corresponding
 254 to that of fresh FDNPP fuel (²³⁵U = 3.7 atomic %). We considered also spent FDNPP UO₂ fuel of
 255 reactor 3 containing 0.7 wt% of Pu [41], MOX fuel of the reactor 3 containing 0.05 g·g⁻¹ of Pu
 256 [41], and a natural zircon with a U weight concentration around 1 wt% (determined in zircon
 257 crystals from the Saranac Prospect, Bancroft, Ontario) [42].

258

259 3.1.1. Calculation of the number of detected α -tracks

260 The theoretical number of α -tracks detected by α -autoradiography techniques, n_α , for a
 261 solid sample is given by Eq. (5)

$$262 \quad n_\alpha = \frac{\pi}{12} \times K \times N_A \times t_{ini} \times \eta_\alpha \times \eta'_\alpha \times \rho_P \times d_P^3 \times \left[\frac{C_U}{M_U} \times \left(\sum_{i=234,235,238} (X_{iU} \times \lambda_{iU}) + \right. \right. \\ \left. \left. \sum_{j=1}^n (X_{Udp,j} \times \lambda_{Udp,j}) \right) + \frac{C_{Pu}}{M_{Pu}} \sum_{i=239,240} (X_{iPu} \times \lambda_{iPu}) \right] \quad (5)$$

264

265 Where K is the detector efficiency (ratio of the number of registered α tracks and the theoretical α
 266 emitted), N_A is the Avogadro constant, t_{ini} is the integration time processed for experimental
 267 analysis (10 days) (s), η_α is the transmission coefficient of α -nuclei within the particle, η'_α
 268 transmission coefficient of α -nuclei between the particle and the detector, ρ_P is the particle density
 269 (g·cm⁻³), d_P is the equivalent particle diameter (cm), C_U is the weight concentration of U in the
 270 particle (0.88 g·g⁻¹ for pure UO₂, $\sim 10^{-3}$ g·g⁻¹ for zircon), C_{Pu} is the weight concentration of Pu in
 271 the particle (~ 0.05 g·g⁻¹ for MOX), M_U is the molar mass of U, M_{Pu} is the molar mass of Pu, X_{iU} is
 272 the total isotope abundance of ²³⁴U, ²³⁵U and ²³⁸U isotopes in U, X_{iPu} is the total isotope abundance
 273 of ²³⁹Pu and ²⁴⁰Pu isotopes in Pu, $X_{Udp,j}$ is the abundance of U decay products:

$$274 \quad \sum_{j=1}^n (X_{Udp,j} \times \lambda_{Udp,j}) = 6 \times X_{^{234}\text{U}} \times \lambda_{^{234}\text{U}} = 6 \times X_{^{238}\text{U}} \times \lambda_{^{238}\text{U}}$$

275 equilibrium or negligible if the U had been chemically purified (U from FDNPP), λ is the

276 disintegration constant of the radionuclides (s^{-1}). According to the literature, the efficiency (K) of
 277 IP for α detection is 64% (derived from [27] and [33] based on ^{239}Pu), while it reaches 51% for the
 278 BeaQuant[®] device (derived from [37]).

279 The determination of the exact value of the product $\eta_\alpha \times \eta'_\alpha$ was not carried out in this work
 280 because it is difficult to estimate. It depends on (1) the particle composition which contained the
 281 α -emitting radionuclides, (2) the distribution of the α -emitting radionuclides within the particles
 282 (i.e. homogeneously distributed or not, as inclusions, etc.), (3) the radionuclide itself (particle type
 283 and emission energy) and (4) the collodion layer thickness into which particles are trapped [37].
 284 Three transmission values were assumed for calculation: 0.01, 0.1 and 1, which correspond to low,
 285 medium and high transmissions respectively.

286

287 3.1.2. Calculation of the fission-tracks (FT) detected number

288 The theoretical number of FT (n_f) observed in 2π -steradian can also be estimated for the
 289 same types of particles according to Eq. (6) modified equation from [43]:

$$290 \quad n_{FT} = \frac{\pi}{6} \times K_{dry} \times N_A \times t_{ir} \times \eta_{FT} \times \eta'_{FT} \times \rho_P \times$$

$$291 \quad d_P^3 \times \phi \times \left(\frac{X_{235U} \times C_U \times \sigma_{235U}}{M_U} + \frac{X_{239Pu} \times C_{Pu} \times \sigma_{239Pu}}{M_{Pu}} \right) \quad (6)$$

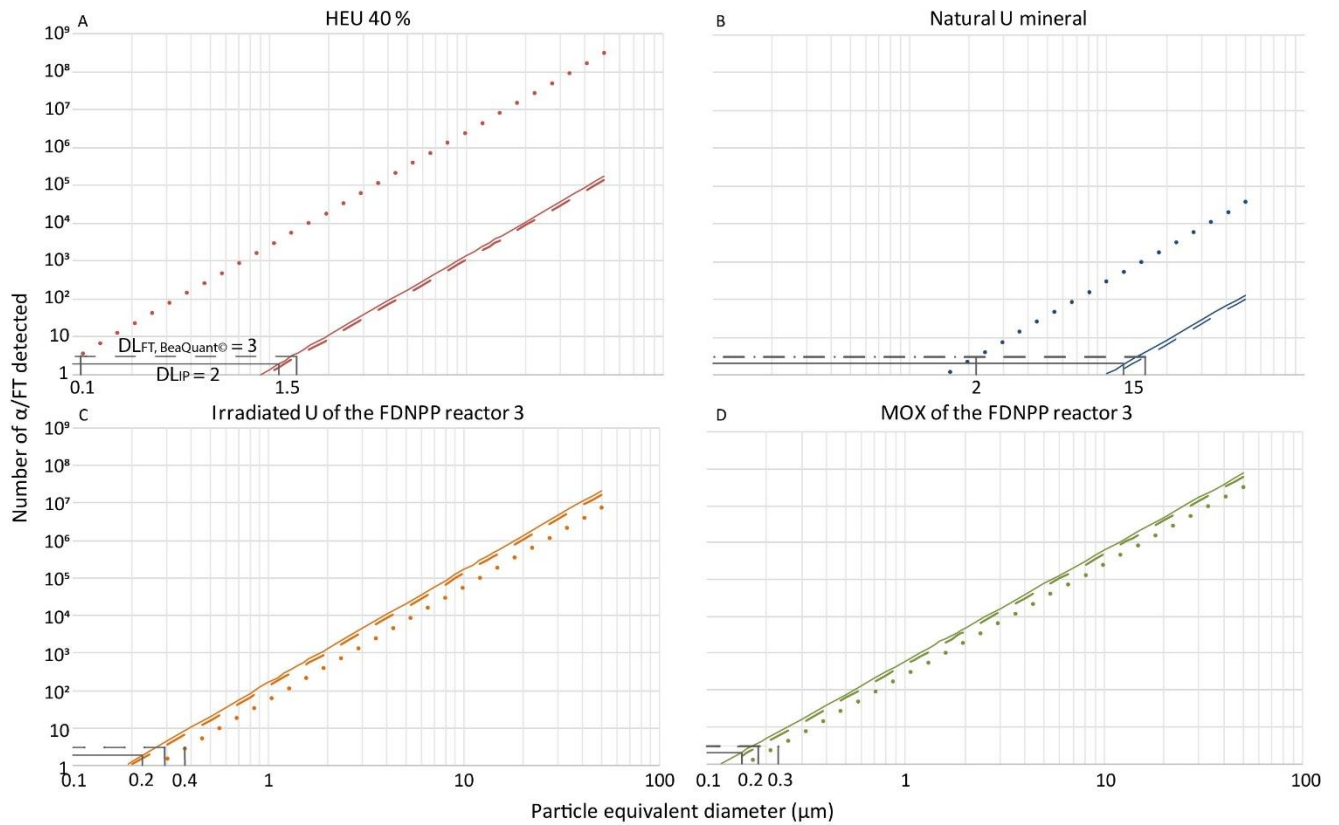
292 Where K_{dry} is the track registration efficiency of Lexan[®], which is estimated to 96 % \pm 4 % [44],
 293 N_A is the Avogadro constant, t_{ir} is the irradiation time processed for experimental analysis (s), η_{FT}
 294 is the transmission coefficient of fission fragment within the particle, η'_{FT} is the transmission
 295 coefficient of fission fragment between the particle and the detector (the product $\eta_{FT} \times \eta'_{FT}$ is
 296 determined to be 1), ρ_P is the particle density ($g \cdot cm^{-3}$), d_P is the equivalent particle diameter (cm),
 297 ϕ is the thermal neutron flux (1.00×10^{15} neutrons $\cdot cm^{-2}$) provided by the TRIGA reactor, σ is the

298 fission cross section under thermal neutrons, ($5.80 \times 10^{-22} \text{ cm}^2$ for ^{235}U and $7.42 \times 10^{-22} \text{ cm}^2$ for
 299 ^{239}Pu), $X_{235\text{U}}$ is the total isotope abundance of ^{235}U in U, $X_{239\text{Pu}}$ is the total isotope abundance of
 300 ^{239}Pu in Pu, C_U is the weight concentration of U in the particle ($0.88 \text{ g}\cdot\text{g}^{-1}$ for pure UO_2 , $\sim 10^{-3} \text{ g}\cdot\text{g}^{-1}$
 301 1 for zircon), C_{Pu} is the weight concentration of Pu in the particle ($\sim 0.05 \text{ g}\cdot\text{g}^{-1}$ for MOX), M_U is the
 302 molar mass of U, M_{Pu} is the molar mass of Pu.

303

304 **3.1.3. Comparison of the α -autoradiography and FT methods theoretical**
 305 **performance for the actinide-bearing particles of interest**

306 These calculations are applied on elemental compositions chosen previously. Results are
 307 plotted in **Fig. 2**.



308

309 **Fig. 2** Graphical representation of theoretical calculation results for $\eta_\alpha \times \eta'_\alpha = 1$ (high transmission)

310 expressed as the number of detected α -tracks/FT plotted against particle size, particle composition

311 and technique used, with logarithmic scales for both axes. A: HEU 40 %; B: Natural U mineral;
312 C: Irradiated U from the FDNPP reactor 3; D: MOX of the FDNPP reactor 3 (for graphs C and D
313 the burnup average values determined by [41] are considered). Colored solid lines represent results
314 for IP; colored dashed line represent results for BeaQuant[®]; colored dotted lines represent results
315 for FT. The black lines represent the detection limits of each method in our analytical conditions
316 (see **Table 1**). Results for $\eta_\alpha \times \eta'_\alpha = 0.1$ (medium transmission) and $\eta_\alpha \times \eta'_\alpha = 0.01$ (low
317 transmission) are given in supplementary information B.

318

319 The theoretical calculations demonstrate the impact of the transmission coefficient and
320 particle size and composition on detecting of α -emissions. For a transmission coefficient of the α
321 nuclei equal to 1 ($\eta_\alpha \times \eta'_\alpha = 1$), the theoretical calculations show that only HEU particles larger
322 than 1 μm can be detected by IP and the BeaQuant[®], whereas HEU particles larger than 0.1 μm
323 can theoretically be detected with the FT method. Regarding the naturally occurring U particles,
324 they can be detected by all of three methods respectively with a full transmission of the α -nuclei
325 for equivalent diameters larger than 15 μm for IP and BeaQuant[®], and larger than 2 μm for FT. By
326 contrast, detection of irradiated U particles and reactor 3 MOX particles with equivalent diameters
327 larger than 0.2 μm is possible even with the lowest transmission factor ($\eta_\alpha \times \eta'_\alpha = 0.01$) by means
328 of the three tested methods. Actually, as explained by [45], a small fraction of Pu in U (in the 10^{-3}
329 – 10^{-2} range) strongly increases the number of α -emissions.

330 Accordingly, the FT method may be the method offering the best chance of detecting U
331 bearing-particles from FDNPP with an equivalent diameter greater than 0.3 μm .

332

333 **3.2. Experimental results**

334 Results of the comparison of the three localisation methods for particles that create FT or
 335 α -track clusters above the detection limits are summarized in **Table 1**. Regarding the BeaQuant[®],
 336 we gathered the results obtained with the two-acquisition methods (methods 1 and 2), as the same
 337 post-processing was implemented for the two methods.

338

339 **Table 1** Results obtained with the three-localisation methods tested in this study. “/” corresponds
 340 to sample not analysed. For IP and BeaQuant[®] values of background noise and detection limits
 341 reported here are the averages for all of our experiments for all samples. Background noise and
 342 detection limits for the FT, IP and BeaQuant[®] methods are expressed in number of fission tracks
 343 observed per cluster, number of α -tracks observed per cluster, and counts per pixel, respectively.

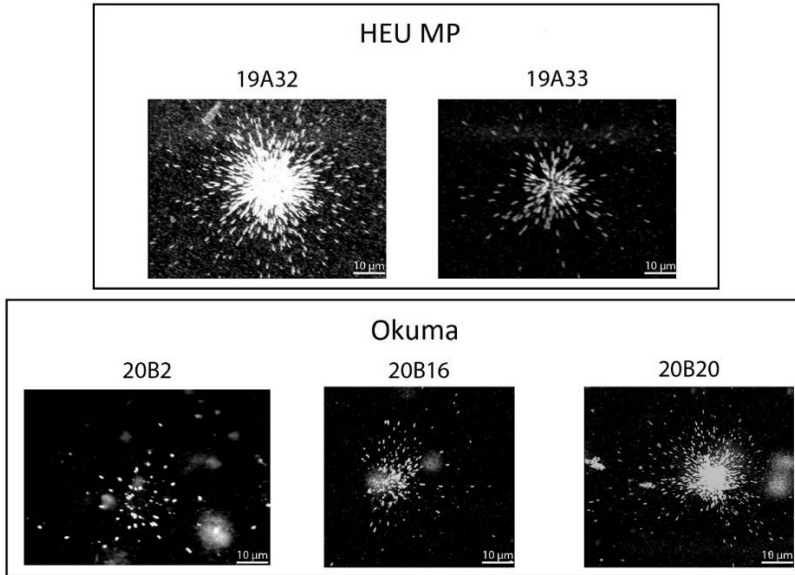
Localisation method	Background noise	Detection limit (DL) for a cluster	Number of clusters detected for samples					
			HEU MP 19A32	HEU MP 19A33	Okuma 20B2	Okuma 20B16	Okuma 20B20	Control
FT	1	3	4	4	3	2	1	/
IP	2	6	0	/	9	1	14	/
BeaQuant [®]	1	3	/	0	0	3	1	1

344

345 Background noise is determined for parts of the detector without radioactive particles. The
 346 detection limit values are calculated according to the Eq. (7):

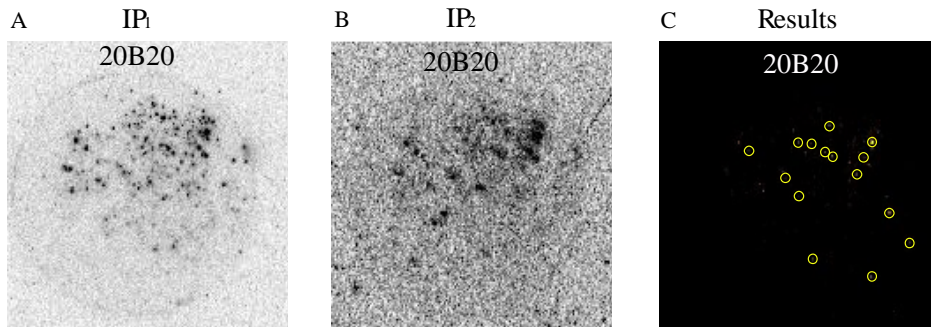
$$347 \quad DL = mean_{background} + 3 \times RSD \quad (7)$$

348 The FT method allows locating particles that contain fissile nuclei for both HEU MP and
 349 Okuma disks (**Fig. 3**). The advantage of this method that it is insensitive to the background
 350 associated with the high activity of ¹³⁷Cs.



351
 352 **Fig. 3** Images of large FT clusters (more than 30 tracks) observed for HEU MP sample disks and
 353 Okuma sample disks. Observations were made with a binocular glass ($\times 6.5$).
 354

355 The IP method revealed pixel clusters with significant PSL above DL only for Okuma disks
 356 (**Fig. 4.c**).



357
 358 **Fig. 4** A: Autoradiography image of IP1 without correction; B: Autoradiography image of IP2
 359 without correction; C: Autoradiography image after processing which allowed localising
 360 significant clusters of pixels. Yellow dots correspond to clusters of pixels above DL.
 361

362 The BeaQuant[®] has a homogeneous background whatever the sample. Clusters are
363 observed for the Okuma sample (disks 20B16, and 20B20) and for the Control sample (IAEA-
364 472). The detection of one pixel above background for the Control sample, which has a relatively
365 low ¹³⁷Cs activity (Supplementary information C), suggests that the influence of the β-γ activity is
366 not fully removed. The background observed could be link to radon levels induce by long exposure
367 time and Lexan[®] disks. However, this method did not allow the detection of α-emitting particles
368 for the HEU MP and for the disk 20B2 of the Okuma.

369

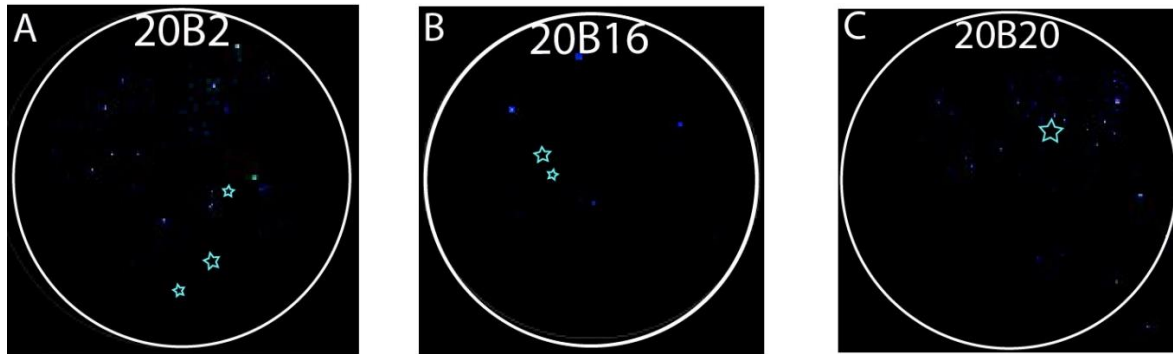
370 **3.3. Comparison of methods for the localisation of pure U-bearing particles and** 371 **radioactive particles in a sediment sample from FDNPP**

372 Here we compared the performance of the methods applied to the HEU MP samples that
373 contain only pure micrometric U particles. For these samples, only the FT method allowed the
374 detection of particles as shown in **Table 1**. The inefficiency of IP and BeaQuant[®] methods may be
375 associated with the particle diameter correlated to the transmission coefficient. As demonstrated
376 in **Fig. 2**, for transmission coefficients respectively equal to 1, 0.1, and 0.01, the equivalent
377 diameter of particles should be higher than 1, 2, and 5 μm to be detected. Accordingly, for detecting
378 pure HEU particles (²³⁵U atomic abundance of 40%), only the FT method was efficient. Indeed,
379 SIMS measurements show that most of the HEU particles have diameters between 0.25 to 0.4 μm.
380 This can be explained by (1) the fact that particles are too small (in the micron range) and thus do
381 not contain enough α-emitting nuclei, (2) the transmission coefficient or yield for IP and
382 BeaQuant[®] methods are too low, or (3) a fading effect may limit their detection by IP [46].
383 Consequently, α activity could not be detected within 10 days.

384 The three methods were also applied to the sediment sample Okuma collected near the
385 FDNPP. As explained previously, aliquots of the sample were deposited on three Lexan® disks.
386 The FT method enabled the detection of three particles in the disk 20B2, two particles in the disk
387 20B16 and one in disk 20B20.

388 However, the IP method did not allow the detection of α -emitting particles at the same
389 locations on the FT disks, although several clusters of pixels with an intensity higher than the
390 detection limit were detected at other locations (**Fig. 5**). The pixel clusters (set of pixels with a
391 spatial resolution of 150 dpi (169 μm)) can be induced by β - γ emissions of radio-caesium and by
392 radon levels which may impact background levels with long exposure time, that were not fully
393 removed by the data treatment. It cannot be mineral particles that contain naturally occurring U as
394 these particles would also have been detected by means of the FT method.

395



396

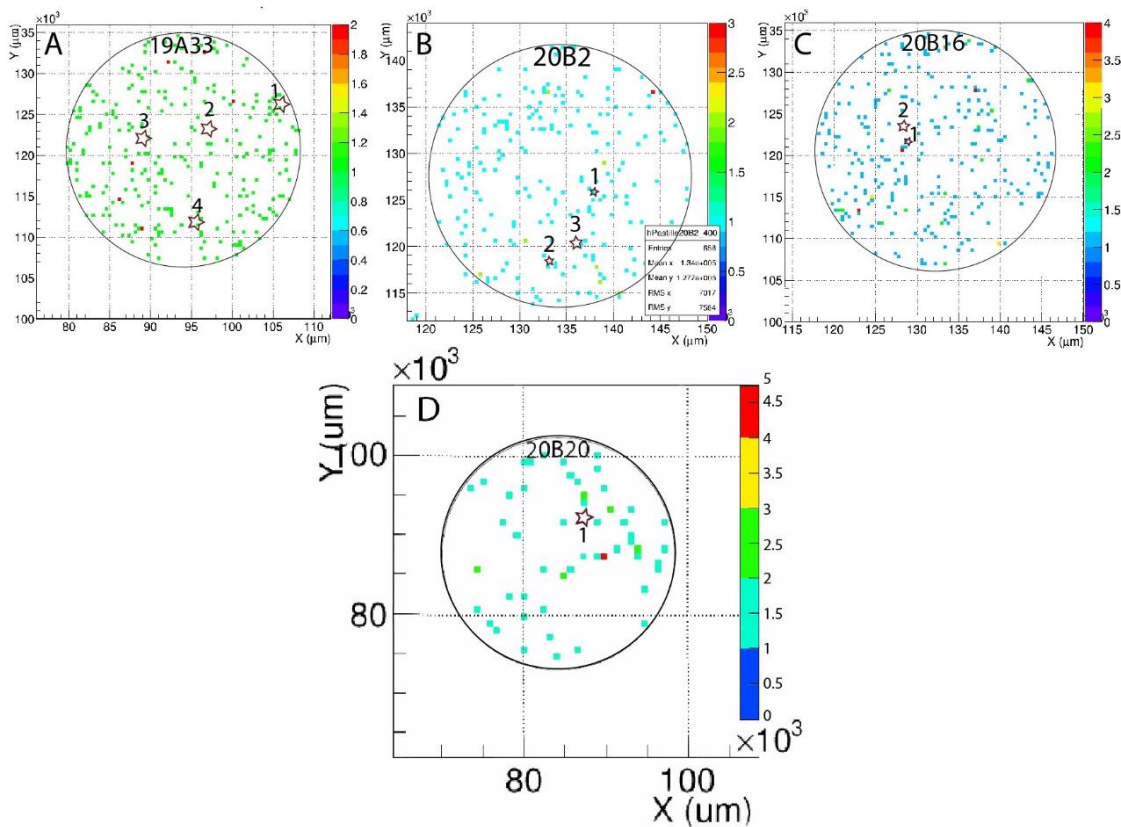
397 **Fig. 5** Comparison between FT and IP results for disks 20B20 (A), 20B16 (B), and 20B2 (C). Star
398 shapes correspond to the location of FT clusters and blue points correspond to clusters of pixels
399 detected by IP (reading with a resolution of 150 dpi (169 μm)).

400

401 The BeaQuant® device showed few pixels with values above the DL, i.e. with 3 or 4 counts
402 (pixel resolution: 400 μm). However, again, when results are compared to those of the FT method,

403 no correlation is observed whereas any types of α -emitter-bearing particles would have been
 404 detected with the FT method. So false pixel detection on the Control sample and blank samples
 405 may suggest that the BeaQuant[®] settings and/or data treatment does not fully remove β
 406 contributions (**Fig. 6**). Actually, considering the higher ^{137}Cs activity of the Fukushima samples
 407 compared to that of Control sample, we cannot exclude the possibility of an increase of the
 408 background due to the β emissions of radio-cesium as observed with IP.

409 To summarise, no correspondence was observed between on one side the pixels above the
 410 DL recorded with the BeaQuant and the clusters of α -tracks above DL with the IP method and on
 411 the other side the localisation of FT clusters that exceed the DL.



412
 413 **Fig. 6** Comparison between FT and BeaQuant[®] results (400 × 400 μm²). A: HEU MP sample; B:
 414 Okuma disk 20B2; C: Okuma disk 20B16; D: Okuma disk 20B20. Purple star shapes correspond

415 to the location of FT clusters and coloured pixels correspond to counts detected with the
416 BeaQuant®.

417

418 Combination of theoretical calculation and experimental comparison of the three
419 localisation methods revealed that only the FT method allows locating U-bearing particles for the
420 Okuma and HEU MP samples. Several hypotheses can be put forward to explain the absence of
421 particle detection by the two autoradiography methods:

422 (1) Particles were too small, and consequently α -activities were too low to induce
423 detectable α activity per surface unit (IP pixel size $169 \times 169 \mu\text{m}^2$; BeaQuant® pixel
424 size $400 \times 400 \mu\text{m}^2$).

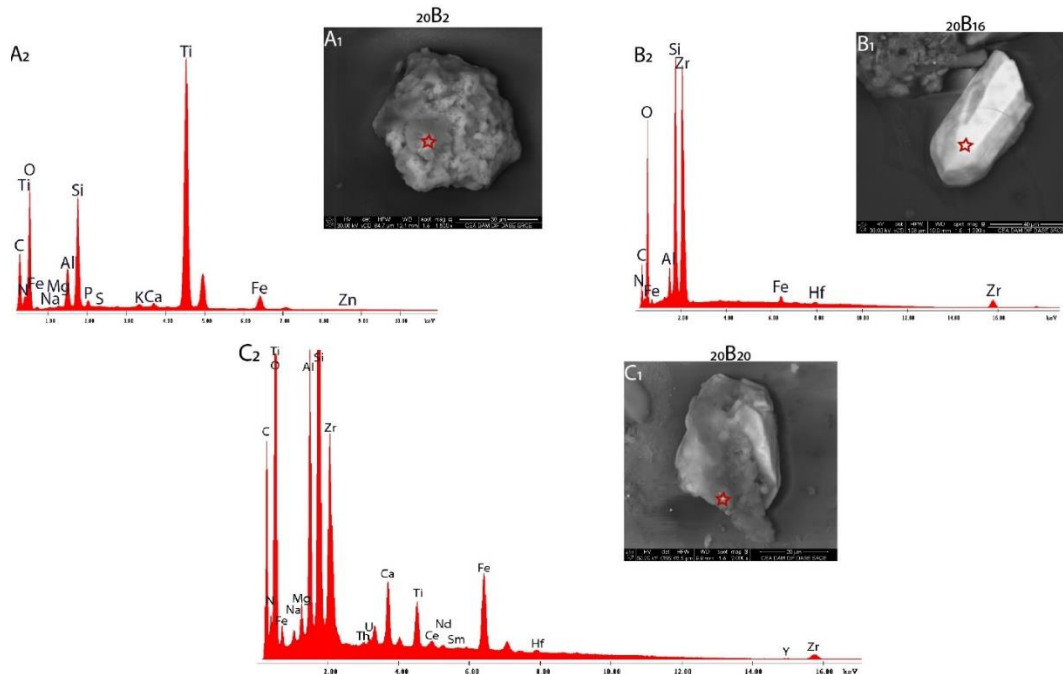
425 (2) The layer of organic polymer (collodion) used to fix the sediment particles may
426 significantly reduce the number of α emerging from the surface of the sample disks
427 (low η'_α). It should be noted that the collodion thickness is not controlled or known.

428 (3) The self-absorption phenomenon may be too high if the U is embedded in the form of
429 nanoparticles within larger radioactive microparticles mainly made of silica for
430 instance (low η_α). Actually, according to the literature, α -emissions from actinides have
431 a penetration of only a few μm in U-rich minerals [47].

432 (4) A fading effect may occur for the IP method, which can lead to loss of information for
433 low activities with the two-week long exposure time of this study [46]. Nevertheless,
434 such a long exposure time was mandatory to increase the probability of detecting
435 micrometric particles.

436 The size and U concentration of the three particles that gave large clusters of FT in disks
437 20B2, 20B16 and 20B20 were evaluated by SEM-EDS. The particle of the disk 20B2 (**Fig. 7a1**)

438 has a pseudo-spherical shape with a diameter of $\sim 40 \mu\text{m}$. The particle on the disk 20B16 (**Fig. 7a₂**)
 439 has a rod shape with a length of $\sim 50 \mu\text{m}$ in the longest dimension. The particle on the disk 20B20
 440 (**Fig. 7a₃**) has no specific shape with a length of $\sim 40 \mu\text{m}$. These particles contain elements that are
 441 abundant in many minerals including Si, O, Al and Fe (**Fig. 7b₁, b₂ and b₃**) although they also
 442 include the following elements: Ti, Mg, Na, K, P and S for disk 20B2, and Zr for disks 20B16 and
 443 20B20.
 444



445
 446 **Fig. 7** SEM images and EDS spectra of the three particles that produces large clusters (A₁, A₂, B₁,
 447 B₂, C₁ and C₂) are presented. A₁: SEM image of the particle of the disk 20B2; A₂: EDS spectrum
 448 of the particle of the 20B2 disk; B₁: SEM image of the zircon of disk 20B16; B₂: EDS spectrum
 449 of zircon of the disk 20B16; C₁: SEM image of the zircon of the disk 20B20; C₂: EDS spectrum
 450 of zircon of the disk 20B20. Red stars represent the spots where EDS spectra were performed.
 451

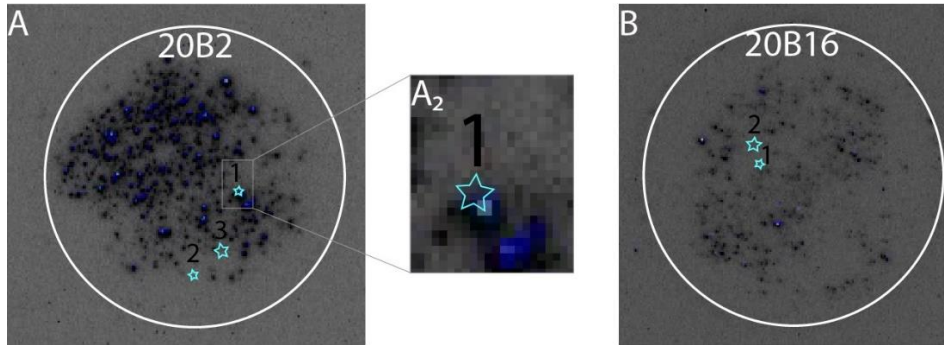
452 Given their elemental composition and morphology, it is assumed that the particles detected
453 in disks 20B16 and 20B20 are zircons. In contrast, the elemental composition of the particle
454 observed on disk 20B2 is very close to that of the FDNPP-originating particles observed by [4,
455 10]). However, U was not detected by EDS in the particle found in disk 20B2 despite the
456 observation of a large FT cluster, which may indicate that its concentration remains below the EDS
457 detection limit, i.e. less than 1 wt%.

458 In the current analytical conditions and in the investigated samples, among the three
459 methods tested, only the FT method allows localising U-bearing particles (natural or
460 anthropogenic). However, as shown by SEM-EDS results on disks 20B16 and 20B2, the FT
461 method itself does not distinguish between natural U particles and those that may originate from
462 FDNPP. Coupling of FT imaging and IP β - γ imaging could allow differentiating between
463 naturally-occurring U in minerals and anthropogenic U-bearing particles from FDNPP. Indeed, the
464 correlation of a FT cluster with an IP pixel cluster of radio-caesium β - γ signals would strongly
465 suggest that the corresponding particle originates from FDNPP. This method was implemented on
466 these three disks. Instead of the IP data treatment described in Eq. 4, the IP1 autoradiography
467 image was treated in order to detect large clusters induced by β - γ emission. The obtained β - γ
468 images were then superimposed with the FT imaging.

469 In the case of the zircon particles, no correspondence with β signals was found (**Fig. 8B**),
470 whereas in the case of the potential anthropogenic particle a coincidence was clearly observed
471 (**Fig. 8A**). Therefore, this particle has great chances to be anthropogenic, released by FDNPP.
472 Further investigations will be performed on that particle in order to identify its origin. These
473 preliminary results suggest that coupling of FT and β - γ IP can be an alternative technique to
474 determine the source of U-bearing particles. Such result could be improved by coupling FT and

475 BeaQuant® in β mode thanks to its better pixel resolution and less sensitivity to the ambient
476 background.

477



478

479 **Fig. 8** Superimposition of the localisation FT and β - γ cluster respectively for disks 20B2 and
480 20B16 (A and B). Light blue stars represent FT clusters.

481

482 **4. Conclusions**

483 The analytical and experimental results of this study demonstrate that under the chosen
484 analytical conditions and the selected samples the fission track method is more effective than the
485 two tested α -autoradiography methods to detect and localise U-bearing particles.

486 In this study, HEU MP, as well as particles containing fissile nuclei (natural, or
487 anthropogenic U) in a sediment sample collected in the vicinity of the FDNPP were only recorded
488 by the fission track method. However, the current study also demonstrated that, for a sediment
489 sample, this method alone does not allow to distinguish (1) particles released by FDNPP which
490 contain fragments of nuclear fuel from (2) mineral particles which contain naturally-occurring U.
491 Indeed, our experiments showed that natural zircon minerals with a diameter larger than 10 μm
492 were also detected by means of the FT method. On the contrary, the two α -radiography methods

493 did not provide any results for our samples. This may probably be explained by a too high auto-
494 absorption (1) either in the collodion layer, which is nevertheless required to prevent
495 contamination of the detector by radioactive particles, or (2) possibly within the particles
496 themselves. Nevertheless the results obtained for the two α -radiography methods confirm that
497 presently the developed data treatment did not enable full removal of the contribution of the β
498 and/or γ emitters on the α images. Thus, the implementation of a method coupling the FT efficiency
499 for the detection of α -emitters and the IP efficiency for the detection of β - γ -emitters was tested in
500 order to attempt the discrimination between naturally occurring U-bearing particles and
501 anthropogenic particles. Results are promising because they enabled the distinction between zircon
502 particles and a particle that could potentially come from FDNPP. Restricting the analysis to
503 particles detected by both methods will definitely avoid isolating U-rich minerals and significantly
504 increase the probability of identifying anthropogenic radioactive particles.

505 To conclude, this study opens new perspective for the detection and localisation of U-
506 bearing particles in sediment/soil samples. The combined methodology will be applied to more
507 sediment and soil samples collected in areas located within the main radioactive contamination
508 plume of FDNPP in order to isolate U-bearing particles. The methodology can also probably be
509 improved by coupling the FT method with the BeaQuant® instrument because of its better
510 sensitivity and spatial resolution than IP.

511 **Acknowledgements**

512 Aurélie Diacre received a PhD fellowship from CEA (Commissariat à l’Energie Atomique et aux
513 Energies Alternatives, France). Sample collection was supported by MITATE Lab (CNRS
514 International Research Project) and AMORAD projects (Programme d’Investissements d’Avenir

515 en Radioprotection et Sûreté Nucléaire, grant no. ANR-11-RSNR-0002). The Ai4R company staff
516 is also acknowledged for the time invested in the current project, including that for optimising
517 acquisitions in α mode and data post-processing. The authors are also grateful to Gabriel Lambrot
518 for formal analysis and Hugues Haedrich for his help to identify the different experimental
519 methods.

520 **References**

- 521 1. Kashparov VA (2003) Hot Particles at Chernobyl. 10
- 522 2. Salbu B, Krekling T, Oughton DH, et al (1994) Hot particles in accidental releases from
523 Chernobyl and Windscale nuclear installations. *Analyst* 119:125–130.
524 <https://doi.org/10.1039/AN9941900125>
- 525 3. Sandalls FJ, Segal MG, Victorova N (1993) Hot particles from Chernobyl: A review. *Journal*
526 *of Environmental Radioactivity* 18:5–22. [https://doi.org/10.1016/0265-931X\(93\)90063-D](https://doi.org/10.1016/0265-931X(93)90063-D)
- 527 4. Abe Y, Iizawa Y, Terada Y, et al (2014) Detection of Uranium and Chemical State Analysis
528 of Individual Radioactive Microparticles Emitted from the Fukushima Nuclear Accident
529 Using Multiple Synchrotron Radiation X-ray Analyses. *Anal Chem* 86:8521–8525.
530 <https://doi.org/10.1021/ac501998d>
- 531 5. Adachi K, Kajino M, Zaizen Y, Igarashi Y (2013) Emission of spherical cesium-bearing
532 particles from an early stage of the Fukushima nuclear accident. *Scientific reports* 3:2554.
533 <https://doi.org/10.1038/srep02554>
- 534 6. Imoto J, Ochiai A, Furuki G, et al (2017) Isotopic signature and nano-texture of cesium-rich
535 micro-particles: Release of uranium and fission products from the Fukushima Daiichi
536 Nuclear Power Plant. *Scientific Reports* 7:5409. [https://doi.org/10.1038/s41598-017-05910-](https://doi.org/10.1038/s41598-017-05910-z)
537 [z](https://doi.org/10.1038/s41598-017-05910-z)
- 538 7. Furuki G, Imoto J, Ochiai A, et al (2017) Caesium-rich micro-particles: A window into the
539 meltdown events at the Fukushima Daiichi Nuclear Power Plant. *Scientific Reports* 7:1–10.
540 <https://doi.org/10.1038/srep42731>
- 541 8. Kurihara Y, Takahata N, Yokoyama TD, et al (2020) Isotopic ratios of uranium and caesium
542 in spherical radioactive caesium-bearing microparticles derived from the Fukushima Dai-ichi
543 Nuclear Power Plant. *Scientific Reports* 10:1–10. [https://doi.org/10.1038/s41598-020-](https://doi.org/10.1038/s41598-020-59933-0)
544 [59933-0](https://doi.org/10.1038/s41598-020-59933-0)

- 545 9. Kurihara E, Takehara M, Suetake M, et al (2020) Particulate plutonium released from the
546 Fukushima Daiichi meltdowns. *Science of The Total Environment* 743:140539.
547 <https://doi.org/10.1016/j.scitotenv.2020.140539>
- 548 10. Martin PG, Griffiths I, Jones CP, et al (2016) In-situ removal and characterisation of uranium-
549 containing particles from sediments surrounding the Fukushima Daiichi Nuclear Power Plant.
550 *Spectrochimica Acta Part B: Atomic Spectroscopy* 117:1–7.
551 <https://doi.org/10.1016/j.sab.2015.12.010>
- 552 11. Martin PG, Louvel M, Cipiccia S, et al (2019) Provenance of uranium particulate contained
553 within Fukushima Daiichi Nuclear Power Plant Unit 1 ejecta material. *Nature*
554 *Communications* 10:1–7. <https://doi.org/10.1038/s41467-019-10937-z>
- 555 12. Martin PG, Jones CP, Cipiccia S, et al (2020) Compositional and structural analysis of
556 Fukushima-derived particulates using high-resolution x-ray imaging and synchrotron
557 characterisation techniques. *Scientific Reports* 10:1636. <https://doi.org/10.1038/s41598-020-58545-y>
558
- 559 13. Ochiai A, Imoto J, Suetake M, et al (2018) Uranium Dioxides and Debris Fragments Released
560 to the Environment with Cesium-Rich Microparticles from the Fukushima Daiichi Nuclear
561 Power Plant. *Environ Sci Technol* 52:2586–2594. <https://doi.org/10.1021/acs.est.7b06309>
- 562 14. Satou Y, Sueki K, Sasa K, et al (2018) Analysis of two forms of radioactive particles emitted
563 during the early stages of the Fukushima Dai-ichi Nuclear Power Station accident.
564 *Geochemical Journal* 52:137–143. <https://doi.org/10.2343/geochemj.2.0514>
- 565 15. Satou Y, Sueki K, Sasa K, et al (2016) First successful isolation of radioactive particles from
566 soil near the Fukushima Daiichi Nuclear Power Plant. *Anthropocene* 14:71–76.
567 <https://doi.org/10.1016/j.ancene.2016.05.001>
- 568 16. Igarashi Y, Kogure T, Kurihara Y, et al (2019) A review of Cs-bearing microparticles in the
569 environment emitted by the Fukushima Dai-ichi Nuclear Power Plant accident. *Journal of*
570 *Environmental Radioactivity* 205–206:101–118.
571 <https://doi.org/10.1016/j.jenvrad.2019.04.011>
- 572 17. Aarkrog A (1971) Radioecological Investigations of Plutonium in an Arctic Marine
573 Environment. *Health Physics* 20:31–47
- 574 18. Eriksson M, Ljunggren K, Hindorf C (2002) Plutonium hot particle separation techniques
575 using real-time digital image systems. *Nuclear Instruments and Methods in Physics Research*
576 *Section A: Accelerators, Spectrometers, Detectors and Associated Equipment* 488:375–380.
577 [https://doi.org/10.1016/S0168-9002\(02\)00438-2](https://doi.org/10.1016/S0168-9002(02)00438-2)
- 578 19. Jiménez-Ramos MC, García-López J, García-Tenorio R, García-León M (2009)
579 Characterization of terrestrial hot particles from the Palomares accident using destructive and
580 non-destructive analytical techniques. *Radioprotection* 44:345–350.
581 <https://doi.org/10.1051/radiopro/20095067>

- 582 20. Jiménez-Ramos MC, García-Tenorio R, Vioque I, et al (2006) Presence of plutonium
583 contamination in soils from Palomares (Spain). *Environmental Pollution* 142:487–492.
584 <https://doi.org/10.1016/j.envpol.2005.10.030>
- 585 21. Pöllänen R, Ketterer ME, Lehto S, et al (2006) Multi-technique characterization of a
586 nuclearbomb particle from the Palomares accident. *Journal of Environmental Radioactivity*
587 90:15–28. <https://doi.org/10.1016/j.jenvrad.2006.06.007>
- 588 22. Donohue DL (2002) Peer Reviewed: Strengthened Nuclear Safeguards. *Anal Chem* 74:28 A-
589 35 A. <https://doi.org/10.1021/ac021909y>
- 590 23. Jaegler H, Pointurier F, Onda Y, et al (2018) Plutonium isotopic signatures in soils and their
591 variation (2011-2014) in sediment transiting a coastal river in the Fukushima Prefecture,
592 Japan. *Environmental Pollution* 240:167–176. <https://doi.org/10.1016/j.envpol.2018.04.094>
- 593 24. Esaka KT, Esaka F, Inagawa J, et al (2004) Application of Fission Track Technique for the
594 Analysis of Individual Particles Containing Uranium in Safeguard Swipe Samples. *Jpn J Appl*
595 *Phys* 43:L915. <https://doi.org/10.1143/JJAP.43.L915>
- 596 25. Sardini P, Angileri A, Descostes M, et al (2016) Quantitative autoradiography of alpha
597 particle emission in geo-materials using the BeaverTM system. *Nuclear Instruments and*
598 *Methods in Physics Research Section A: Accelerators, Spectrometers, Detectors and*
599 *Associated Equipment* 833:15–22. <https://doi.org/10.1016/j.nima.2016.07.003>
- 600 26. Furuki G, Imoto J, Ochiai A, et al (2017) Caesium-rich micro-particles: A window into the
601 meltdown events at the Fukushima Daiichi Nuclear Power Plant. *Scientific Reports* 7:1–10.
602 <https://doi.org/10.1038/srep42731>
- 603 27. Haudebourg R, Fichet P (2016) A non-destructive and on-site digital autoradiography-based
604 tool to identify contaminating radionuclide in nuclear wastes and facilities to be dismantled.
605 *J Radioanal Nucl Chem* 309:551–561. <https://doi.org/10.1007/s10967-015-4610-7>
- 606 28. Chartin C, Evrard O, Onda Y, et al (2013) Tracking the early dispersion of contaminated
607 sediment along rivers draining the Fukushima radioactive pollution plume. *Anthropocene*
608 1:23–34. <https://doi.org/10.1016/j.ancene.2013.07.001>
- 609 29. IAEA (2019) Environmental Sample Particle Analysis Interlaboratory Comparison
- 610 30. Bonnet T, Comet M, Denis-Petit D, et al (2013) Response functions of imaging plates to
611 photons, electrons and 4He particles. *Review of Scientific Instruments* 84:103510.
612 <https://doi.org/10.1063/1.4826084>
- 613 31. Chen B, Zhuo W, Kong Y (2011) Identification and counting of alpha tracks by using an
614 imaging plate. *Radiation Measurements* 46:371–374.
615 <https://doi.org/10.1016/j.radmeas.2011.01.002>

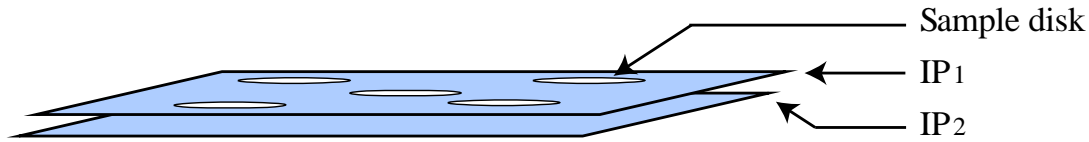
- 616 32. Billon S, Sardini P, Leblond S, et al (2018) MAUD PROJECT-Comparative study of 3
617 Digital Autoradiography Techniques for characterization: Gas Detector -Solid Scintillation
618 Detector -Phosphor Screens
- 619 33. Rahman NM, Iida T, Yamazawa H, Moriizumi J (2006) Determination of Alpha Particle
620 Detection Efficiency of an Imaging Plate (IP) Detector. *Jpn J Health Phys* 41:272–278.
621 <https://doi.org/10.5453/jhps.41.272>
- 622 34. Fichet P, Bresson F, Leskinen A, et al (2012) Tritium analysis in building dismantling process
623 using digital autoradiography. *J Radioanal Nucl Chem* 291:869–875.
624 <https://doi.org/10.1007/s10967-011-1423-1>
- 625 35. Radulović V, Kolšek A, Fauré A-L, et al (2018) Qualification of heavy water based
626 irradiation device in the JSI TRIGA reactor for irradiations of FT-TIMS samples for nuclear
627 safeguards. *Nuclear Instruments and Methods in Physics Research Section A: Accelerators,*
628 *Spectrometers, Detectors and Associated Equipment* 885:139–144.
629 <https://doi.org/10.1016/j.nima.2017.12.046>
- 630 36. Donnard J, Berny R, Carduner H, et al (2009) The micro-pattern gas detector PIM: A multi-
631 modality solution for novel investigations in functional imaging. *Nuclear Instruments and*
632 *Methods in Physics Research Section A: Accelerators, Spectrometers, Detectors and*
633 *Associated Equipment* 610:158–160. <https://doi.org/10.1016/j.nima.2009.05.186>
- 634 37. Billon S, Sardini P, Angileri A, et al (2020) Quantitative imaging of ²²⁶Ra ultratrace
635 distribution using digital autoradiography: Case of doped celestines. *Journal of*
636 *Environmental Radioactivity* 217:106211. <https://doi.org/10.1016/j.jenvrad.2020.106211>
- 637 38. Donnard J, Arlicot N, Berny R, et al (2009) Advancements of labelled radio-pharmaceutics
638 imaging with the PIM-MPGD. *J Inst* 4:P11022–P11022. [https://doi.org/10.1088/1748-](https://doi.org/10.1088/1748-0221/4/11/P11022)
639 [0221/4/11/P11022](https://doi.org/10.1088/1748-0221/4/11/P11022)
- 640 39. Donnard J, Thers D, Servagent N, Luquin L (2009) High Spatial Resolution in β -Imaging
641 With a PIM Device. *IEEE Transactions on Nuclear Science* 56:197–200.
642 <https://doi.org/10.1109/TNS.2008.2005673>
- 643 40. Angileri A, Sardini P, Beaufort D, et al (2020) Mobility of daughter elements of ²³⁸U decay
644 chain during leaching by In Situ Recovery (ISR): New insights from digital autoradiography.
645 *Journal of Environmental Radioactivity* 220–221:106274.
646 <https://doi.org/10.1016/j.jenvrad.2020.106274>
- 647 41. Nishihara K, Iwamoto H, Suyama K (2012) Estimation of fuel compositions in Fukushima-
648 Daiichi nuclear power plant. 202. <https://doi.org/JAEA-Data/Code-2012-018>
- 649 42. Nasdala L, Hanchar JM, Rhede D, et al (2010) Retention of uranium in complexly altered
650 zircon: An example from Bancroft, Ontario. *Chemical Geology* 269:290–300.
651 <https://doi.org/10.1016/j.chemgeo.2009.10.004>

- 652 43. Kalsi PC, Sawant PD, Ramaswami A, Manchanda VK (2007) Track etching characteristics
653 of polyester track detector and its application to uranium estimation in seawater samples. J
654 Radioanal Nucl Chem 273:473–477. <https://doi.org/10.1007/s10967-007-6845-4>
- 655 44. Khan HA, Durrani SA (1972) Efficiency calibration of solid state nuclear track detectors.
656 Nuclear Instruments and Methods 98:229–236. [https://doi.org/10.1016/0029-
657 554X\(72\)90103-6](https://doi.org/10.1016/0029-554X(72)90103-6)
- 658 45. Jaegler H, Pointurier F, Onda Y, et al (2019) Method for detecting and characterising
659 actinide-bearing micro-particles in soils and sediment of the Fukushima Prefecture, Japan. J
660 Radioanal Nucl Chem 321:57–69. <https://doi.org/10.1007/s10967-019-06575-w>
- 661 46. Muuri E, Sorokina T, Donnard J, et al (2019) Electronic autoradiography of ^{133}Ba particle
662 emissions; diffusion profiles in granitic rocks. Applied Radiation and Isotopes 149:108–113.
663 <https://doi.org/10.1016/j.apradiso.2019.04.026>
- 664 47. Angileri A, Sardini P, Donnard J, et al (2018) Mapping ^{238}U decay chain equilibrium state
665 in thin sections of geo-materials by digital autoradiography and microprobe analysis. Applied
666 Radiation and Isotopes 140:228–237. <https://doi.org/10.1016/j.apradiso.2018.06.018>
- 667

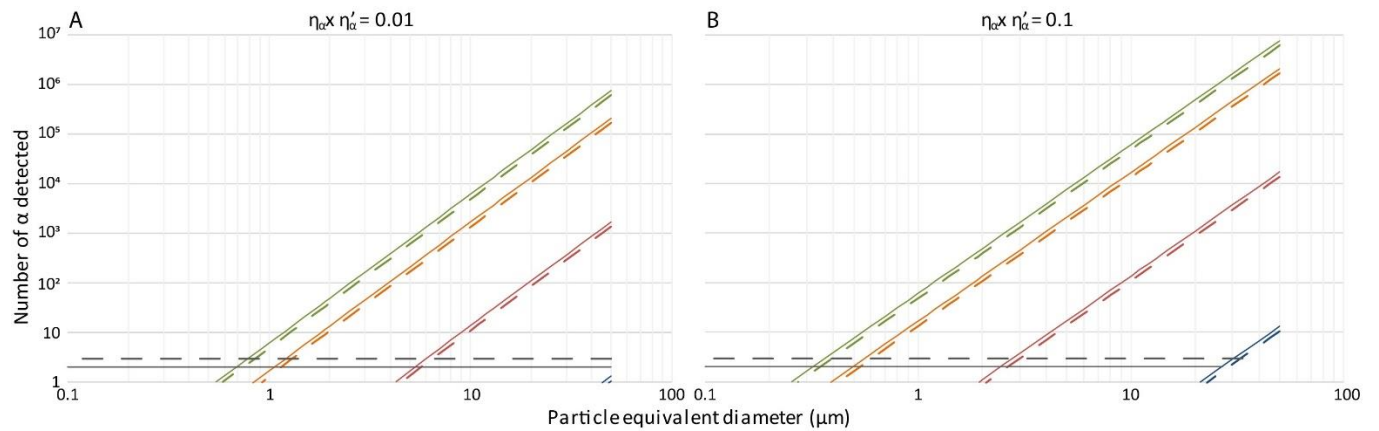
668

Supplementary information

669

670 **A:** Scheme of imaging plate experiments.

671



672

673 **B:** Graphical representation of theoretical calculation results for products A. $\eta_{\alpha} \times \eta'_{\alpha} = 0.1$ (medium674 transmission) and B. $\eta_{\alpha} \times \eta'_{\alpha} = 0.01$ (low transmission) expressed as the number of alpha/FT

675 detected as a function of particle size, composition and technique used, at logarithmic scale.

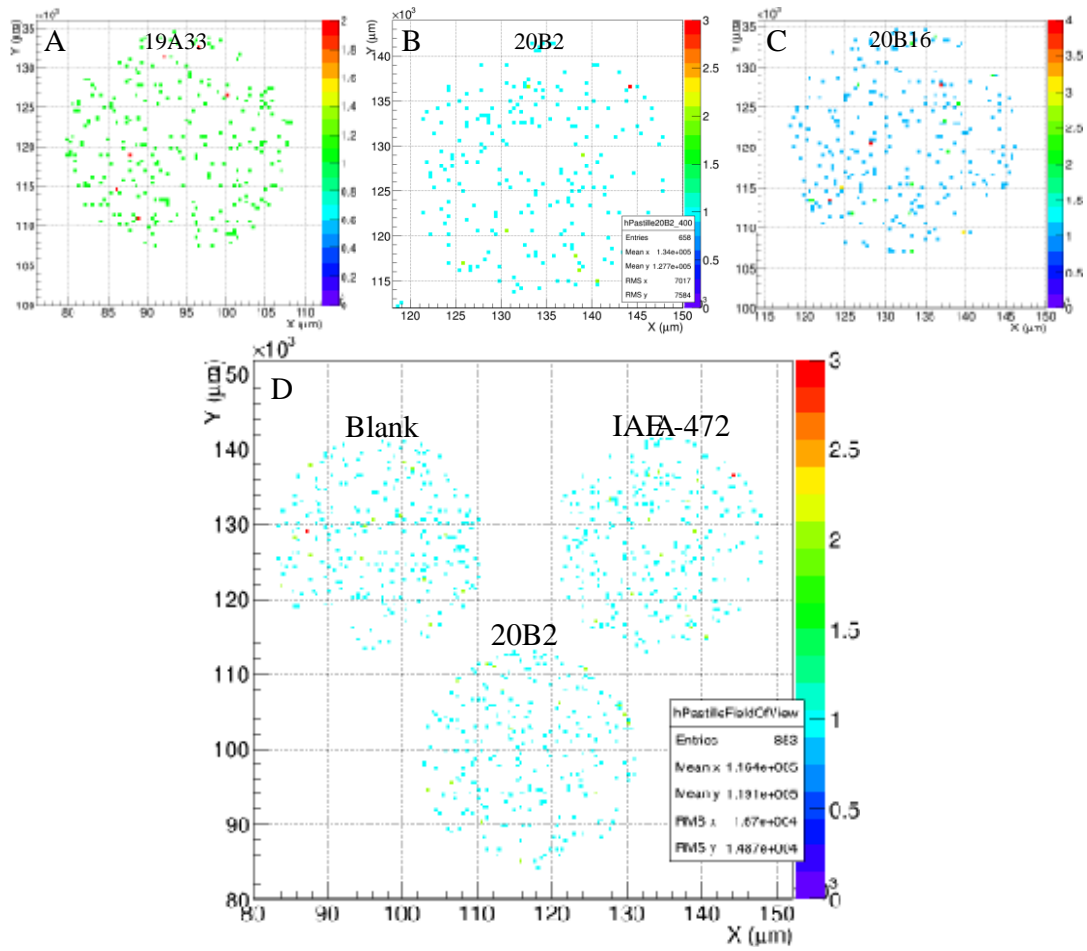
676 Colored solid line represent results for IP, colored dashed line represent results for BeQuant®.

677 These same black lines represent the detection limits of each method in our analytical conditions.

678 Green line is for MOX of the FDNPP reactor 3; Orange line is for Irradiated U of the FDNPP

679 reactor 3; Pink line is for HEU 40%; Blue line is for Natural U mineral.

680



681 C: BeQuant® results after the application of low amplitude filter A. Quality control disk 19A33;

682 Fukushima samples; B. 20B2 (two acquisitions) and C. 20B16; D. Blank and IAEA-472 samples.

683